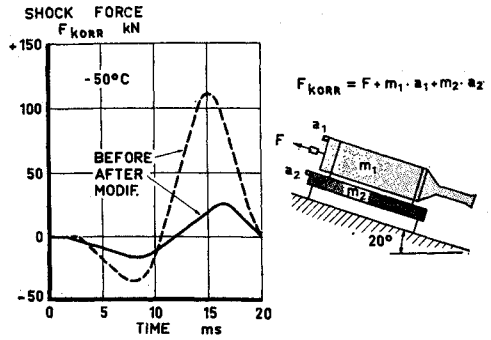

Fig. 6 Ignition shock history.

Ignition shock

The sudden displacement of the fuel to the forward end of the tank when the piston breaks away produced a positive (forward) shock with a magnitude of more than 110 kN, Fig. 6. The shock was calculated from taped measurements with two accelerometers and the ordinary thrust transducer. The engine was then oriented in the most unfavorable firing position with the combustion chamber slightly downward and at the lowest temperature where the ullage is maximum. This magnitude of shock could not be tolerated by the customer due to missile equipment sensitivity. It was, however, impossible to weaken the break away seals on the piston because this could cause an accidental break during the environmental testing.

A computer program was set up for a model of the transient behavior at ignition and this showed that an increase of the initial tank nitrogen pressure and a longer burning time of the ignition pellets would reduce the shock to a tolerable level, but still keep the thrust build up time less than 250 msec. Tests with these modifications showed that the shock dropped to 25 kN and, thus, the specified limit was met with a good margin.

Combustion instability

The injector is based on a design developed by the Swedish Research Institute of National Defense and has 20 unlike doublets impinging on a splashplate, Fig. 7. It had shown excellent performance during the component testing, but installed in the complete propulsion system the fuel pressure drop across the injector had to be decreased in order to get a sufficient combustion efficiency. An instability at 1000 Hz was introduced by this change.

It was shown analytically that this instability was due to a coupling between the feed system and the injector where the liquid freestream time was of significant importance. By intensive component testing of the injector parameters, and by comparing the results with those obtained at actual engine firings, the injector characteristics could be plotted very clearly, Fig. 8. The figure shows that the way to get a stable combustion with a high c^* efficiency was to decrease the freestream time, either by increasing the velocity, increasing the pressure

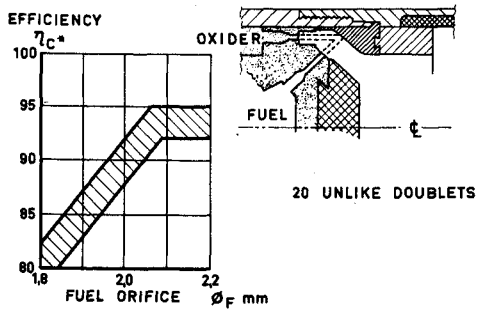

Fig. 7 Injector principle.

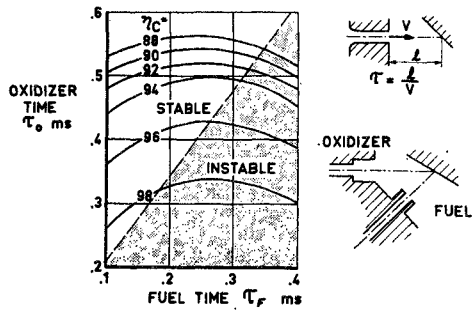

Fig. 8 Injector characteristic.

drop, or by decreasing the freestream length. The stable part of the diagram becomes more narrow with higher performance and to allow for the manufacturing tolerances, the requirements were restricted to around 97% c^* efficiency.

Transverse Deflection of Guided Projectile Tail Fins during Deployment

WILLIAM R. CHADWICK*
U.S. Naval Weapons Laboratory, Dahlgren, Va.

Introduction

AN important problem in the development of guided projectiles is the design of suitable high aspect ratio tail fins which deploy automatically under the influence of low spin as the projectile leaves the gun. In order to accommodate the fins in the gun barrel and to achieve the most rearward possible fin location (to maximize airframe stability) attention has been directed mainly at tail fins which deploy rearwards from their stowed position in the projectile afterbody (Fig. 1). Deployment tests at the Naval Weapons Lab.

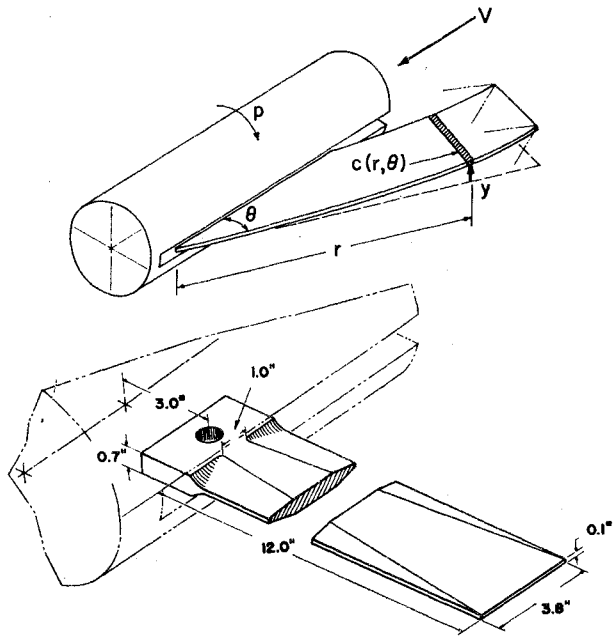

Fig. 1 Tail-fin geometry; 8-in. guided projectile.

Received December 11, 1972; revision received May 1, 1973.
Index category: Launch Vehicle and Missile Technology.
* Research Aerospace Engineer.

using the 8-in. Naval gun commenced in 1969. Several tests, employing blades with aspect ratio 3 and root thickness 0.4 in., were unsuccessful and the root thickness was increased to 0.7 in. ($t/c = 0.18$). A number of firings have been entirely successful with the increased root thickness, at launch velocities up to 1800 fps and at spin rates up to 12 cps. At 17 cps, however, the fins experienced a clear root bending failure. This Note attempts to explain the observed failure by investigating the blade's transverse deflection mode under the influence of Coriolis bending forces and steady aerodynamic forces which arise due to elastic deformation, roll damping and static angle of attack. It will be seen that the essential problem is one of extremely rapid structural divergence. Unsteady aerodynamic forces are not considered. The launch Mach number is 2.

Analysis

The differential equation for the blade deployment angle θ is

$$d^2\theta/dt^2 = p^2 \cos\theta(Dr_0 + \sin\theta) \tag{1}$$

where D denotes the ratio of first to second mass moments about the point of rotation, which is located (Fig. 1) at the distance $r_0 = 3$ in. from the projectile spin axis. In terms of θ, the deployment rate is

$$\dot{\theta} = (2)^{1/2}p[Dr_0 \sin\theta + \tfrac{1}{4}(1 - \cos 2\theta)]^{1/2} \tag{2}$$

with a maximum value at $\theta = \pi/2$ of $(2)^{1/2}p$ for $D = \frac{1}{8}$ in.$^{-1}$

In addition to the centrifugal acceleration of the blade mass elements there is also a Coriolis acceleration. This arises in the classical Coriolis sense as twice the vector cross product of the projectile spin (p) with the tangential velocity ($r,\dot{\theta}$). The Coriolis force/unit length, producing upward flexure in Fig. 1, is therefore

$$P_c(r,\theta) = 2pr\dot{\theta} \cos\theta\bar{\rho}s(r) \tag{3}$$

where $s(r)$ is the blade cross section and $\bar{\rho}$ the material density.

Aerodynamic loads due to the Coriolis induced bending, together with aerodynamic roll damping forces and air loads due to possible projectile incidence, will further increase blade flexure.

Steady supersonic linear wing theory, applied to a yawed rectangular wing of semi-infinite span, is used to estimate the blade-section lift curve slope $a(r,\theta)$.[1] The exposed planform increases with θ, as shown, and this has been taken into account by multiplying $a(r,\theta)$ by the instantaneously exposed local blade chord $c(r,\theta)$. Accordingly, the aerodynamic loading at the spanwise station (r) at the opening angle (θ) is approximated by

$$P_a(r,\theta) = \tfrac{1}{2}\rho V^2 c(r,\theta)a(r,\theta)\alpha(r,\theta) \tag{4}$$

where $\alpha(r,\theta)$ is the local angle of attack

$$\alpha(r,\theta) = \alpha_0 + (p/V)(r_0 + r\sin\theta) + (dy/dr)\cos\theta \tag{5}$$

The blade is assumed clamped during the entire deployment cycle along the root chord which corresponds to $\theta = 90°$. Plane elastic bending theory is used and twist of the blade sections is neglected. The equation describing the transverse vibration is

$$(\partial^2/\partial r^2)[EI(r)\,\partial^2 y/\partial r^2] + \bar{\rho}s(r)\partial^2 y/\partial t^2 = 2pr\dot{\theta}\cos\theta\bar{\rho}s(r) + \tfrac{1}{2}\rho V^2 c(r,\theta)a(r,\theta)\alpha(r,\theta) \tag{6}$$

where positive deflection (y) is defined as upward flexing of the blade shown in Fig. 1. With $y(r,0) = 0$ and the boundary conditions

$$y(0,t) = (\partial y/\partial r)(0,t) = 0$$
$$(\partial^2 y/\partial r^2)(1,t) = (\partial^3 y/\partial r^3)(1,t) = 0 \tag{7}$$

Eq. (6) has been solved using the method of finite differences with $\Delta r = 1.0$ in. and $\Delta t = 0.00001$ sec.

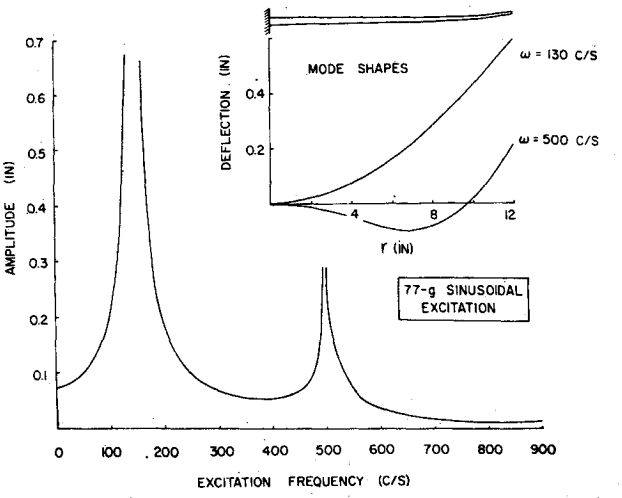

Fig. 2 Variation of tip deflection amplitude with forced vibration frequency.

Discussion

Two checks were performed on the method used for solving the partial differential equation. First, the numerical solution was shown to agree with the known theoretical solution for a cantilever beam having constant sectional properties and vibrating freely following the release of a concentrated end load. Second, harmonic forcing was applied along the length of the blade and tip deflection amplitude plotted against excitation frequency. The results, confirmed by vibration tests, are shown in Fig. 2 and indicate first and second natural frequencies in pure bending of 130 and 500 cps.

Figures 3 and 4 are examples of the general solution of the transverse vibration equation. Projectile spin is 20 cps. Figure 3 shows blade tip deflection and integrated span loading against time. The tip motion is directly in phase with the Coriolis force. Maximum deflection (assuming continuous elastic bending) is 2.6 in. at 12 mil sec with $\theta = 45°$. The total blade loads are then 1150 lb (aerodynamic), 460 lb (Coriolis) and 400 lb (direct transverse inertia). For $\theta > 45°$ both the Coriolis force ($\dot{\theta}\cos\theta$) and the aerodynamic force ($dy/dr\cos\theta$) begin to decrease and the transverse motion of the blade reverses. At $\theta = 120°$ (full deployment), the Coriolis force vanishes and the subsequent vibrations occur at the first

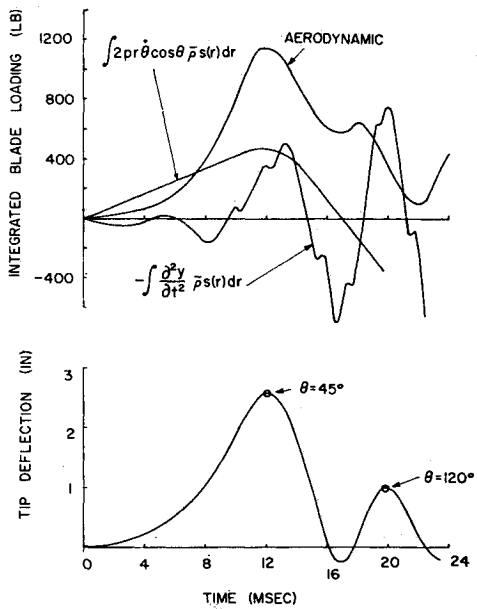

Fig. 3 Variation of tip deflection and integrated blade loading with time.

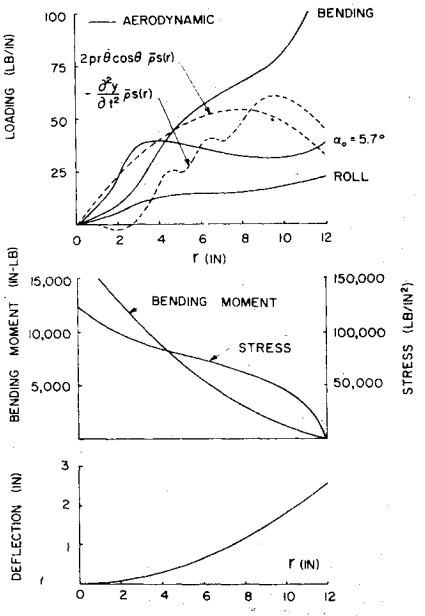

Fig. 4 Spanwise variation of blade loading, bending moment, stress and deflection.

natural frequency. Vibrations at a frequency higher than the fundamental are also indicated in Fig. 3.

Figure 4 shows the spanwise variation of blade loading, bending moment, stress and deflection at maximum loading. Thus, while the Coriolis force initiates the elastic deformation, the excessive flexural divergence is due mainly to the large aerodynamic force associated with tip flexure. With forward opening tail fins, on the other hand, the aerodynamic loads due to bending act to minimize blade flexure and under these conditions substantially reduced stress levels occur.

Finally, it should be pointed out that the results shown in Fig. 4 adequately account for the structural failures mentioned previously (yield-stress of the test blades $\approx$ 70,000 lb/in.^{2}).

Conclusions

High aspect ratio rearward opening tail fins deployed under the influence of projectile spin may experience excessive bending stresses at the root. The problem is one of large transverse blade flexure initiated by Coriolis inertia forces. The high stress levels encountered, however, are due mainly to the associated buildup of large aerodynamic forces which develop as the blade tip sections bend in the supersonic airstream.

References

[1] Ferri, A., *Elements of Aerodynamics of Supersonic Flows*, MacMillan, New York, 1949, pp. 350–383.

Durability Tests of a 5-cm-diam Ion Thruster System

SHIGEO NAKANISHI*
NASA Lewis Research Center, Cleveland, Ohio

Presented as Paper 72-1151 at the AIAA/SAE 8th Joint Propulsion Specialist Conference, New Orleans, La., November 29–December 1, 1972; submitted December 18, 1972; revision received April 23, 1973.

Index category: Electric and Advanced Space Propulsion.

* Aerospace Engineer, Spacecraft Technology Division.

Introduction

AN ion thruster technology program for small mercury bombardment ion thrusters has been in progress at the Lewis Research Center for several years.[1,2] Within this program, a 5-cm-diam thrust-vectorable structurally integrated ion thruster system was designed and developed by the Hughes Research Labs.[3,4] To determine the ultimate life of the system and to pinpoint potential problem areas not discernible in short-term tests, durability tests have been run at the Lewis Research Center. This Note presents some long-term performance results of the Hughes SIT-5 thruster system modified for specific tests at Lewis. Thruster operation exceeding 8000 hr is described with an abridged history of the durability test. The results of the initial 2023 hr of testing performed with a translating screen vector grid are also included. An independent test conducted concurrently on the propellant feed system is described.

Apparatus and Procedure

The SIT-5 (structurally integrated thruster, 5 cm diam) system has a single gas pressurized propellant reservoir which feeds mercury to the porous tungsten vaporizers of the main cathode and the neutralizer. A propellant isolator allows the feed system to operate at neutralizer potential. For the test at Lewis, the propellant reservoir was removed, and the vaporizers were connected to capillary flow tubes. The neutralizer was mounted on an isolated support and oriented to point downstream parallel to the thruster axis. The vertical vacuum test facility was 1.37 m in diameter, 1.83 m tall, and contained a frozen mercury target and a cryowall cooled with liquid nitrogen. The accelerator grid of the thruster was approximately 75 cm above the frozen mercury target when installed. A set of nonmetallic (Fiberfax, 50% Al_2O_3, 50% SiO_2) baffles were installed so that no metallic surface other than the mercury target intercepted the line of sight of the thruster ion beam. Details of the electrical system, automatic digital data acquisition system, protective control system, and test procedures are described in Ref. 5. The thruster was operated open-looped at nominally fixed conditions with minor day-to-day adjustments.

The propellant reservoir, separated from the SIT-5 system, and an identical CIV (cathode-isolator-vaporizer) assembly were durability tested in a vacuum bell jar.[6] A simulated thruster shell without magnets was mounted on the CIV assembly and the discharge current was drawn to a simulated anode connected to the cathode via a discharge power supply. All parameters were maintained at values typical of thruster operation, and the positive high voltage was applied to the simulated anode to provide a realistic test of the isolator.

Results and Discussion

Performance profile

A performance profile of the thruster with electrostatic vector grid after 8022 and 4250 hr of operation is shown in Table 1. The third column shows values obtained with the translating screen vector grid at 2023 hr, the end of its test segment. The performance profile remained relatively constant while each grid type was being tested. Performance differences between grid types were due to differences in grid design. All tests were run at 25 ma beam current, but beam power was higher with the electrostatic vector grid because of the higher net accelerating potential required for proper ion optics. Discharge power was also higher because of lower screen electrode transparency, 28.8% compared with 45.6% in the translating screen grid. Component power requirements were essentially constant throughout the test except for a slight increase in the neutralizer keeper power. Propellant utilization efficiency varied slightly because of variations in propellant flow rate.